351

Shear flow over a translationally symmetric cylindrical bubble pinned on a slot in a plane wall

By JAMES Q. FENG[1,2] AND OSMAN A. BASARAN[1]

[1] Chemical Technology Division, Oak Ridge National Laboratory, Oak Ridge, TN 37831-6224, USA

[2] Department of Chemical Engineering, University of Tennessee, Knoxville, TN 37996, USA

Steady states of a translationally-symmetric cylindrical bubble protruding from a slot in a solid wall into a liquid undergoing a simple shear flow are investigated. Deformations of and the flow past the bubble are determined by solving the nonlinear free-boundary problem comprised of the two-dimensional Navier–Stokes system by the Galerkin/finite element method. Under conditions of creeping flow, the results of finite element computations are shown to agree well with asymptotic results. When the Reynolds number Re is finite, flow separates from the free surface and a recirculating eddy forms behind the bubble. The length of the separated eddy measured in the flow direction increases with Re, whereas its width is confined to within the region that lies between the supporting solid surface and the separation point at the free surface. By tracking solution branches in parameter space with an arc-length continuation method, curves of bubble deformation versus Reynolds number are found to exhibit turning points when Re reaches a critical value Re_c. Therefore, along a family of bubble shapes, solutions do not exist when $Re > Re_c$. The locations of turning points and the structure of flow fields are found to be governed virtually by a single parameter, $We = Ca\,Re$, where We and Ca are Weber and capillary numbers. Two markedly different modes of bubble deformation are identified at finite Re. One is dominant when Re is small and is tantamount to a plain skewing or tilting of the bubble in the downstream direction; the other becomes more pronounced when Re is large and corresponds to a pure upward stretching of the bubble tip.

1. Introduction

The problem of a drop or a bubble in a simple shear flow is of great technological and theoretical interest (e.g. Clift, Grace & Weber 1978). Consequently, it has been the subject of many fundamental fluid mechanics studies to date (e.g. Taylor 1934; Rumscheidt & Mason 1961; Chaffey & Brenner 1967; Cox 1969; Frankel & Acrivos 1970; Barthes & Acrivos 1973; Choi & Schowalter 1975; Flummerfelt 1980). Review articles by Acrivos (1983) and Rallison (1984) summarize both the various theories developed to predict the deformation and break-up of drops and bubbles in shear flows as well as relevant experimental findings. However, most investigations to date have focused on the problem of an isolated drop that is freely suspended in a second fluid and theoretical analyses, following the pioneering work of Taylor (1934), have been restricted to the creeping flow limit. Little is known about the response of supported (sessile or pendant) drops and bubbles in a shear flow – a situation that is of interest in our research and one that is commonly encountered in many multiphase flow processes such as flows on distillation trays and in packed beds among others.
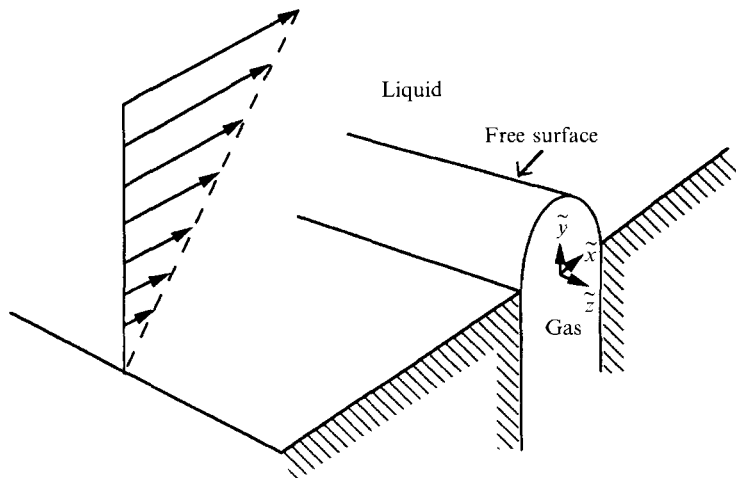
FIGURE 1. A cylindrical bubble protruding from a slot in a solid wall into a liquid undergoing a simple shear flow.

Moreover, the deformation of drops and bubbles in response to a shear flow when inertial effects are important has heretofore been an open problem in fluid mechanics. Accordingly, the goals of this work are to analyse and develop insights into the deformation response of supported bubbles to a shear flow at finite Reynolds numbers.

The main complexity in studying drops and bubbles in flow fields comes from the deformation of the free surface, which gives rise to a free boundary problem. From the physical point of view, at the fluid interface pressure due to uniform surface tension – which likes to maintain the free surface shape of a globular drop or bubble spherical – competes with flow induced stresses – which are almost always non-uniform along the free surface – to distort and set its shape. Indeed, if the flow is strong enough, the distorting stresses can outweigh the pressure due to surface tension and a steady state, which requires a balance of forces on the interface, can no longer be achieved. The usual consequence of loss of steady state is the disintegration of the free surface: in other words, drops or bubbles break into several fragments when they are subjected to very strong flow fields (see, e.g. references cited above). Following previous work on free drops and bubbles, the major task of the present paper on supported bubbles is two-fold: (i) to establish the relationship between the free surface deformation and a given flow field and (ii) to determine the critical values of some measure of the strength of the flow field beyond which a condition of steady state that demands a balance between surface tension and flow induced stresses can no longer be achieved and disintegration of the free surface ensues.

Specifically, we consider a translationally-symmetric cylindrical bubble protruding from a slot in a solid wall into a liquid undergoing a simple shear flow, as shown in figure 1. The axis of the bubble, which lies along the $\tilde{z}$-direction, it taken to be perpendicular to the direction of liquid flow and the bubble is assumed to be pinned to the parallel edges of the slot at the three-phase contact lines (see discussion below). Because of the geometrical complexity and nonlinearities inherent in the present free-boundary problem, solution by means of analytical methods through expansion in terms of conventional functions is both tedious and of limited usefulness. Consequently, we adopt a numerical approach with finite element basis functions and Galerkin's method of weighted residuals (cf. Strang & Fix 1973). Moreover, the Galerkin/finite element method adopted here, in contrast to the boundary integral
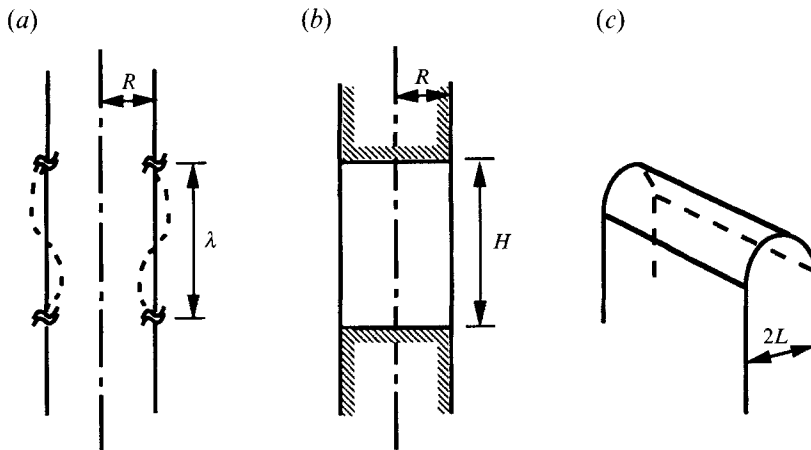
FIGURE 2. (*a*) An infinitely long, free cylindrical column of fluid, (*b*) a cylindrical column of fluid held captive between solid faces, and (*c*) a supported cylindrical column or a fillet of fluid protruding out of a slot.

method which is a popular technique in drop and bubble problems (cf. Pozrikidis 1992), allows solution of the nonlinear Navier–Stokes system so that inertial effects arising from shear flow at finite Reynolds numbers can be explored.

When subject to capillary force alone, an infinitely long, free cylindrical column of liquid of radius R, as in figure 2(*a*), is unstable to axisymmetric shape disturbances that are infinitesimal in amplitude, sinuous, and of wavelength λ greater than the circumference of the cylinder, i.e. $\lambda > 2\pi R$ (Rayleigh 1879). Hence, only when a perfectly cylindrical column of liquid is captive with a length H less than its circumference, i.e. $H < 2\pi R$, as in figure 2(*b*), can it be maintained in the real world (see, e.g. Mason 1970). An infinitely long, supported cylindrical column or a fillet with its contact lines pinned at the edges of a slot, as in figure 1 or 2(*c*), however, can have stable translationally-symmetric equilibrium shapes as long as the interface encloses a volume less than that of a half-cylinder (Brown & Scriven 1980). Hence, not only can supported cylindrical interfaces be observed in everyday life, but they also provide good opportunities for experimental studies owing to the ease with which they can be created in the laboratory.

Aside from translationally-symmetric, supported cylindrical bubbles being physically realizable, the present two-dimensional problem is computationally simpler than and also should retain certain key features of the problem of fully three-dimensional flow past a supported bubble protruding from a circular hole. Indeed, with the advantage in computational overhead that the two-dimensional model holds over the fully three-dimensional model, the two-dimensional problem of shear flow past a supported cylindrical bubble can be a useful prototype of shear flow past a three-dimensional supported bubble when the instability in the third dimension is set aside.

The manner in which a bubble or a drop is attached to the supporting solid surface – in other words, whether the three-phase contact line formed at the intersection between the bubble or drop, the ambient fluid, and the solid surface is pinned or free to move – is an important issue in its own right. In related work on fluid mechanics of drops supported on solid surfaces, Durbin (1988*a*, *b*) determined the wind force that is needed to dislodge a two-dimensional drop adhering to a solid surface and King & Tuck (1993) analysed the problem of upward flow of air that is required to prevent a two-dimensional drop attached to an inclined solid surface from sliding down the plane

under the force of gravity. In contrast to the present paper, these authors made certain assumptions to simplify the underlying fluid mechanical problem. Durbin (1988 a, b) took the ambient fluid flowing past the drop to be inviscid and the liquid inside the drop to be at rest. King & Tuck (1993) took their drop to be a thin liquid layer so that the lubrication approximation holds and the flowing stream of air exerts a tangential stress that is constant in magnitude over the layer. It is noteworthy that in Durbin's papers, contact angle hysteresis (cf. Dussan & Chow 1983) provides the physical mechanism that enables the drop to adhere to the solid surface and makes possible the existence of steady states as the wind force increases. However, the situation for a meniscus to be pinned at three-phase contact lines is equally common in reality, mostly at sharp edges (cf. Oliver, Huh & Mason 1977). Therefore, requiring that the bubble be pinned to the sharp edges of the slot in the supporting wall shown in figure 1 is both physically natural and reasonable.

The physical consequence of pinning a contact line is that the meniscus can then intersect the solid surface at an arbitrary contact angle without causing the migration of the contact line. Of course, this can be true in reality only when the value of the contact angle lies in a certain range. At a mathematically sharp edge, this range of values that the contact angle can have is determined by the Gibbs inequality (Gibbs 1906). The Gibbs inequality was derived from a purely geometrical extension of the familiar Young–Dupré equation, which is a relationship between the equilibrium contact angle and interfacial tensions, but has also been confirmed experimentally by Oliver et al. (1977). Hence, pinning a meniscus at an edge or a corner may be achieved in practice by choosing solid materials of appropriate wettabilities. Moreover, when the contact lines of the bubble are pinned to the edges of the slot, the physical and mathematical statements of the problem are complete even in the absence of gravity and without a concern for a force balance that would have to hold for the bubble to maintain a steady position were its contact lines free to move (cf. Durbin 1988a, b; King & Tuck 1993).

In what follows, §2 presents the set of nonlinear equations and boundary conditions that govern the steady flow of a Newtonian liquid past a deformable translationally symmetric cylindrical bubble and also details the Galerkin/finite element methodology for discretizing and solving the free boundary problem. Section 3 presents computed flow fields and bubble shapes and discusses the evolution of steady shape families of fixed bubble volume in parameter space. The correctness of computational results is reinforced by asymptotic analysis for the deformation of and the flow past a bubble having the volume of a half-cylinder when inertial forces are negligible. By efficiently tracking shape families in parameter space by arc-length continuation methods (e.g. Keller 1977; Abbott 1978), the stability of bubble shapes with respect to translationally symmetric disturbances is inferred by connectivity of the shape families (Iooss & Joseph 1990; Ungar & Brown 1982). Physical insights into the deformation and stability of translationally symmetric, supported bubbles is gained by detailed examination of computed pressure distributions on bubble surfaces, and by decomposition of highly deformed profiles of bubbles into harmonic functions. Section 4 concludes the work with a discussion of some possible applications of the reported calculations to studies of interfacial rheological phenomena.

2. Mathematical formulation and computational analysis

2.1. *Governing equations and boundary conditions*

The system is an incompressible Newtonian liquid of constant viscosity μ and density ρ that is flowing past a cylindrical bubble of fixed volume protruding from a slot in a solid wall, as shown in figure 1. The bubble is composed of a tenuous gas that exerts uniform pressure $\tilde{p}_G$ and negligible viscous drag on the liquid. The interface that separates the bubble and the flowing liquid S_B has constant surface tension σ. The bubble axis lies along the $\tilde{z}$-direction and both the bubble shape and the flow field are the same in every plane of constant $\tilde{z}$. In other words, the problem has translational symmetry with respect to the $\tilde{z}$-direction and the problem domain is the region in the $(\tilde{x}, \tilde{y})$-plane for $\tilde{y} > 0$ that lies above the solid wall and exterior to the bubble volume. The liquid flow is driven by a Couette device with its relatively moving parallel walls far apart. Here the surface with the slot is taken to be the bottom stationary wall of the device and the simple shear flow far from the bubble is characterized by a shear rate G. Variables and equations that follow are made dimensionless by measuring length in units of a characteristic length L that is chosen to be half of the slot width and velocity in units of GL. Moreover, in what follows, variables that appear without a tilde are dimensionless counterparts of those that appear with a tilde.

The fluid motion of the liquid phase satisfies the steady, two-dimensional, incompressible Navier–Stokes system

$$Re\, \boldsymbol{u} \cdot \nabla \boldsymbol{u} = \nabla \cdot \boldsymbol{T}, \tag{1}$$

$$\nabla \cdot \boldsymbol{u} = 0. \tag{2}$$

Here $Re \equiv \rho G L^2 / \mu$ is the Reynolds number and the stress tensor of a Newtonian liquid $\boldsymbol{T} = -p\boldsymbol{I} + \boldsymbol{\tau} = -p\boldsymbol{I} + [\nabla \boldsymbol{u} + (\nabla \boldsymbol{u})^T]$, where p is the pressure, $\boldsymbol{\tau}$ is the viscous stress tensor, and $\boldsymbol{I}$ is the identity tensor. Both the total stress and the pressure are measured in units of μG. The velocity vector $\boldsymbol{u}$ has components $(u, v, w = 0)$ in the x-, y-, and z-directions, respectively. Furthermore, in (1) and throughout the rest of this paper, the relative importance of gravitational force is taken to be negligible compared to inertial, viscous, and surface forces.

An equation is next written that ensures that as the bubble deforms, its volume above the supporting solid wall is constrained to be a fixed amount V_0

$$V = V_0. \tag{3}$$

At the gas bubble–liquid interface, conservation of momentum is expressed by the traction boundary condition

$$\boldsymbol{n} \cdot \boldsymbol{T} = \frac{1}{Ca} \frac{\mathrm{d}\boldsymbol{t}}{\mathrm{d}s} - p_G \boldsymbol{n} \quad \text{on } S_B, \tag{4}$$

where $Ca \equiv \mu G L / \sigma$ is the capillary number, $\boldsymbol{n}$ and $\boldsymbol{t}$ are the local unit normal and tangent vectors to the boundary, and s is arc length along the boundary. Here $\boldsymbol{n}$ points outward from the boundary, i.e. from the liquid to the gas side, $\boldsymbol{t}$ points in the direction of increasing s, and, therefore, $\mathrm{d}\boldsymbol{t}/\mathrm{d}s$ is the two-dimensional curvature. The unknown pressure p_G inside the bubble is of course determined by the volume constraint (3). The bubble shape is unknown *a priori*. However, it is a material surface provided there is no mass transfer across it. The kinematic condition is then simply

$$\boldsymbol{n} \cdot \boldsymbol{u} = 0 \quad \text{on } S_B. \tag{5}$$
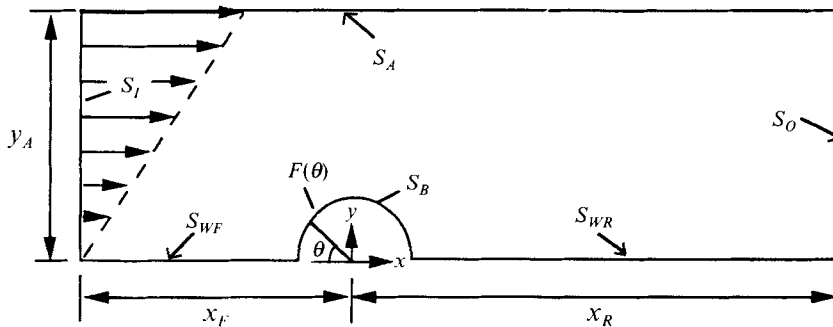
FIGURE 3. Problem domain showing the inflow (inlet) boundary S_I, outflow (outlet) boundary S_O, bubble surface S_B, supporting wall surfaces S_{WF} and S_{WR}, and asymptotic boundary S_A. The figure also defines coordinate system.

Along the stationary solid wall of the slot, to the front S_{WF} and the rear S_{WR} of the bubble, the liquid must obey conditions of no slip and no penetration, namely

$$u = 0 \quad \text{on } S_{WF} \text{ and } S_{WR}. \tag{6}$$

Far from the bubble, the liquid velocity asymptotically approaches that appropriate for a simple shear flow

$$u \to y e_x \quad \text{as } |r| = (x^2 + y^2)^{1/2} \to \infty, \tag{7}$$

where e_x is a unit vector in the x-direction and $r = (x, y, z = 0)$ is the position vector in the (x, y)-plane.

2.2. *Galerkin/finite element analysis*

The Navier–Stokes system (1)–(2) is solved here by the Galerkin/finite element method (GFEM) in the mixed interpolation sense (Huyakorn *et al.* 1978). The solution of the free boundary problem that is comprised of equations (1)–(3) and boundary conditions (4)–(7) is expedited by adopting techniques developed for solving viscous free surface flows by Scriven and coworkers (cf. papers by Kistler & Scriven 1983; Christodoulou & Scriven 1989, 1992; and theses by Christodoulou 1990; de Santos 1991). Some similar techniques have also been used by Basaran (1992) in his study of nonlinear oscillations of viscous drops.

The problem domain depicted in figure 3 is subdivided into a set of quadrilateral elements (see, e.g. Strang & Fix 1973). Each element is mapped onto a unit square in the ξ-η domain, $0 \leqslant \xi \leqslant 1$ and $0 \leqslant \eta \leqslant 1$ (Strang & Fix 1973). On each unit square, the unknown values of the velocity and pressure fields are expressed here in an expansion of biquadratic and linear discontinuous basis functions, respectively. To facilitate simultaneous solution of both the flow field and free surface deformation problems, an elliptic mesh generation scheme (Thompson, Warsi & Mastin 1985) developed by Christodoulou & Scriven (1992) and modified by de Santos (1991) is employed in this paper. The essence of the method is to determine the locations of the nodal or mesh points of the finite element grids by solving a pair of elliptic partial differential equations (PDEs),

$$\nabla \cdot D_1 \nabla \xi = 0, \quad \nabla \cdot D_2 \nabla \eta = 0, \tag{8}$$

where the 'diffusion' coefficients D_1 and D_2 are adjustable functions of position which can be prescribed to meet a particular desire of distribution of nodal or mesh points in the problem domain. For example, if D_1 and D_2 are set to be constants, a uniform mesh is obtained. In order to lessen the computational cost due to solving the mesh

generation equations (8), the subparametric mapping (instead of the isoparametric mapping as commonly used in finite-element computations) for the nodal position unknowns, as put forward by Christodoulou & Scriven (1992), is used here.

Next Galerkin's method is applied by weighting governing equations (1), (2) and (8) with the appropriate finite element basis functions, integrating over the entire physical domain, and applying the divergence theorem to simplify the momentum and elliptic mesh generation equations. The resulting set of nonlinear algebraic equations are further simplified by applying Neumann (natural) and Dirichlet (essential) boundary conditions, as outlined in the following paragraphs.

Because it is impractical to solve a set of nonlinear PDEs on an infinite domain, for finite element computations specific inflow, outflow, and asymptotic boundary conditions that replace boundary condition (7) must be imposed at a finite distance from the bubble. At the inlet boundary S_I, a Dirichlet condition

$$u = ye_x \quad \text{on } S_I \tag{9}$$

is imposed as the inflow boundary condition to the flow domain a distance x_F upstream of the bubble axis, i.e. on the plane $(-x_F, y, 0)$ where $0 \leqslant y \leqslant y_A$ (see figure 3). At the outflow boundary S_O, the Neumann and Dirichlet conditions

$$n \cdot (n \cdot \nabla u) = 0, \quad t \cdot u = 0 \quad \text{on } S_O \tag{10}$$

are imposed on the x- and y-components of the velocity, respectively, as the outflow boundary conditions to the flow domain at a distance x_R downstream of the bubble axis, i.e. on the plane $(x_R, y, 0)$ where $0 \leqslant y \leqslant y_A$. Prescription of boundary conditions on the flow equations (1) and (2) is completed by imposing a Dirichlet condition

$$u = y_A e_x \quad \text{on } S_A \tag{11}$$

along the asymptotic boundary which is simply the plane $(x, y_A, 0)$, where $-x_F \leqslant x \leqslant x_R$.

The GFEM statement of the problem is completed by imposing boundary conditions on the mesh generation equations (8). Here along most boundaries equal arc length spacing of grid points are used and along the free surface either the ξ = constant or the η = constant mesh lines are forced to be orthogonal to the boundary. The former requirement is met by imposing Dirichlet conditions on the relevant mesh generation equations and the latter requirement is met by means of Neumann conditions.

Following the imposition of the boundary conditions, the system of nonlinear algebraic equations $R(\{x_i\}, \{y_i\}, \{u_i\}, \{v_i\}, \{p_i\}, p_G) = R(\omega) = 0$, where $\{x_i\}$ and $\{y_i\}$ are the nodal position values determined by the elliptic mesh equations (8), $\{u_i\}$ and $\{v_i\}$ the nodal values of x- and y-components of velocity, $\{p_i\}$ the nodal values of pressure, and ω is the vector of all nodal unknowns plus p_G, is solved by Newton's method (cf. Ortega & Rheinboldt 1970):

$$J^{(k)} \Delta \omega^{(k+1)} = -R^{(k)}. \tag{12}$$

In (12), $J \equiv \partial R / \partial \omega$ is the Jacobian matrix of partial derivatives and (k) denotes the kth iterate. At each Newton iteration, the resulting linearized system of equations (12) is solved by direct factorization or LU-decomposition of the Jacobian matrix with a modification of Hood's frontal solver (Hood 1976; Walters 1980).

Critical to Newton's method is the initial estimate of the solution which must be accurate enough to fall within the domain of convergence of the method. A convenient start-up solution or initial estimate is obtained here by solving the governing equations under conditions of Stokes flow, $Re = 0$, and vanishingly small capillary number, e.g. $Ca = 0.005$, or, equivalently, when surface tension is very large, such that that the two-
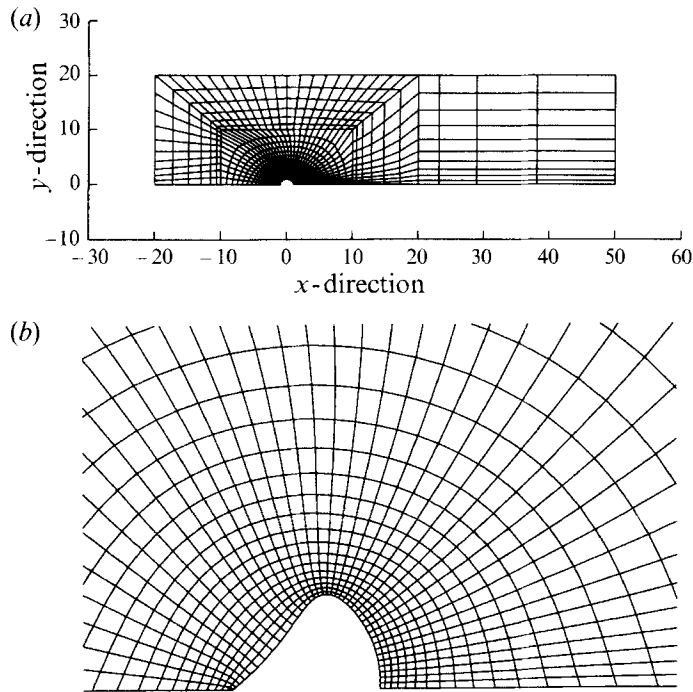
FIGURE 4. Typical tessellation of problem domain by the elliptic mesh generation scheme: (*a*) a view of the entire domain and (*b*) a close-up view of elliptically generated mesh near a deformed free surface.

dimensional free surface is well approximated by an arc of a circle. Thereafter, steady solution families of fixed bubble volume are traced efficiently by first-order continuation (Riks 1972; Keller 1977) either in Re, holding Ca fixed, or in Ca, holding Re fixed. The Jacobian matrix becomes singular at turning points and also certain bifurcation points in parameter space (cf. Iooss & Joseph 1990) and first-order continuation cannot lead to a converged solution. To continue along a solution branch past a turning point (which is the only kind of singular point encountered in this work), an arc-length continuation method (Keller 1977; Abbott 1978) is adopted in this paper.

2.3. *Details of computer implementation*

The algorithm was programmed in FORTRAN and the resulting code was run on an IBM RS6000-320H workstation at the Oak Ridge National Laboratory.

Figure 4 shows a typical mesh obtained with the elliptic mesh generator described earlier. In the results to be reported in the next section, the inlet, outlet, and asymptotic boundaries were so located by choosing $x_F = 20$, $x_R = 50$, and $y_A = 20$ that imposition of boundary condition (9)–(11) at a finite distance from the bubble virtually had no effect on the computed solutions (see below). The domain was divided into 1160 elements. With the mesh used, the numbers of velocity, pressure and nodal location unknowns equalled 9570, 3480 and 2054, respectively. With a total of 15105 unknowns, each Newton iteration took 345.32 s of central processor time. Typically, 5 iterations sufficed to bring the L_2 norm of the error in the solution and residuals within 10^{-5}. Increasing the size of the computational domain or the number of elements deployed in the tessellation changed the location of stability limits or turning points to be reported in §3 by less than 1%.

3. Results and discussion

It is instructive to start with the situation in which the bubble volume is maintained to be equal to that of a half-cylinder $V = V_{1/2}$, which is the maximum volume a stable bubble can have while maintaining translational symmetry under the action of surface tension alone (cf. Brown & Scriven 1980). By virtue of the symmetry a half-cylinder configuration possesses, this case is also amenable to solution by asymptotic analysis in the creeping flow limit. The asymptotic solution reported in §3.1 is indispensable for checking the accuracy of computational results to be reported there. The effect of inertia on bubbles of volume equal to that of a half-cylinder is taken up in §3.2. Because bubbles with volumes less than that of a half-cylinder are expected to be easier to obtain in practice, §3.3 presents a series of computations for bubbles of volumes smaller than that of a half-cylinder. For the sake of completeness, results for bubbles of volumes greater than that of a half-cylinder are also discussed in §3.3.

3.1. *Creeping flow cases: Re = 0 and V = V_{1/2}*

Creeping flows allow considerable theoretical simplifications because inertia forces are negligible. When the amplitude of the deformation of the bubble is small, an analytical formula can easily be obtained correct to first order in Ca for the departure of the unknown shape from the half-cylinder. Following standard procedures of asymptotic analysis, the zeroth-order solution for the streamfunction in polar coordinates (r, θ) is found to be

$$\psi = -\tfrac{1}{4}(r^2 - 1)(1 - \cos 2\theta), \tag{13a}$$

which satisfies the biharmonic equation and all the boundary conditions such as no-slip at solid walls, traction and impenetrability conditions at the circular bubble surface $(r = 1)$, and the far-field condition

$$\psi \to -\tfrac{1}{4}r^2(1 - \cos 2\theta) \quad (r \to \infty). \tag{13b}$$

Here $r = (x^2 + y^2)^{1/2}$ and θ is the polar angle measured from the negative x-axis. With the known zeroth-order solution for the flow field, it is straightforward to determine the stress distribution on the bubble surface, namely pressure

$$p = \sin 2\theta \tag{13c}$$

and viscous normal stress

$$\tau_{rr} = 2\left(\frac{1}{r}\psi_{r\theta} - \frac{1}{r^2}\psi_\theta\right) = -2\sin 2\theta, \tag{13d}$$

where $\psi_\theta \equiv \partial\psi/\partial\theta$, etc. Therefore, to first-order in Ca the bubble shape function is (see figure 3)

$$F(\theta) = 1 - Ca \sin 2\theta. \tag{14}$$

Remarkably, to first-order in Ca the asymptotic solution for the two-dimensional supported bubble predicts the same bubble deformation as that for its three-dimensional counterpart (cf. Taylor 1934) with the deformation parameter and the orientation angle, respectively, given by

$$D \equiv \frac{F_{max} - F_{min}}{F_{max} + F_{min}} = Ca, \quad \alpha = \tfrac{1}{4}\pi = 45°. \tag{15a,b}$$

Here the orientation angle is defined as $\alpha \equiv \pi - \theta_{max}$ with θ_{max} denoting the polar angle at which the interface shape function is a maximum $F = F_{max}$. To first order in Ca, it then follows that $F_{max} = F(\tfrac{3}{4}\pi)$ and $F_{min} = F(\tfrac{1}{4}\pi)$ where F_{min} is the minimum value of F.

Coincidentally, it can be shown that the zeroth-order solution (13a) also holds for a two-dimensional free bubble without the supporting solid wall (cf. Richardson 1968),
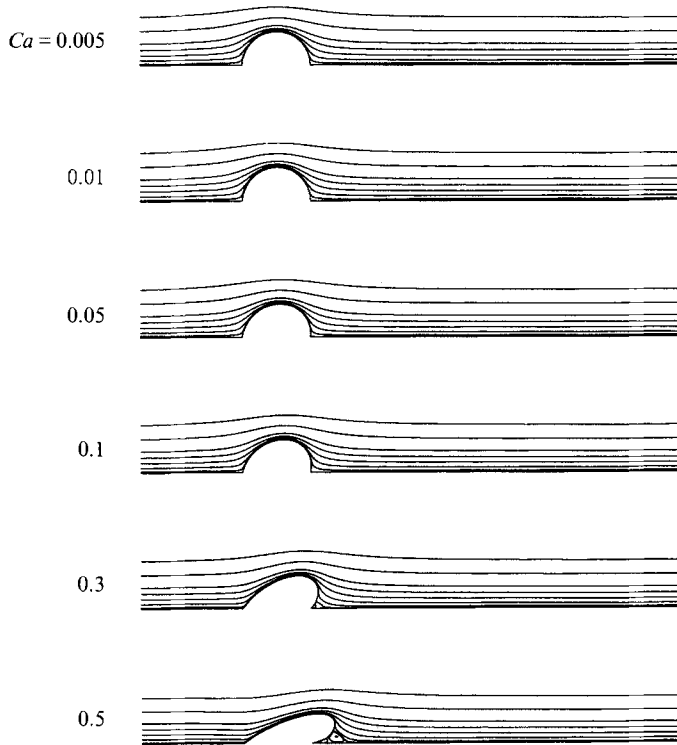
FIGURE 5. Streamlines of flow past a bubble having the volume of a half-cylinder when $Re = 0$ for various Ca values. For illustrative purposes, the values of ψ are chosen to be -0.001, -0.0005, -0.0001, 0, 0.001, 0.01, 0.04, 0.1, 0.2, 0.5, and 1. Not all the streamlines corresponding to negative values of ψ are shown in every case because some of these do not have strong enough recirculating eddies.

a result which is a consequence of the symmetry of the circular shape of the bubble with respect to the $y = 0$ plane. If the analysis is extended to the next order following the domain perturbation procedure, whereas a solution can be obtained for free bubbles in a straightforward way (Zahalak, Rao & Sutera 1987), obtaining a solution for supported bubbles is prohibitively difficult. This is because the deformation of a supported bubble destroys the natural symmetry that exists in the zeroth-order problem. Satisfaction of the condition of zero velocity along the $y = 0$ plane – supporting solid wall – is equivalent to requiring that the flow field and bubble surface be symmetric with respect to the $y = 0$ plane where the deformed surface of the bubble possesses discontinuous surface tangents, or forms corners, at $\theta = 0$ and $\theta = \pi$. The existence of these discontinuities render higher-order domain perturbation analyses impracticable because in principle an infinite number of terms in the standard harmonic expansions must be retained to resolve these corners at the two contact lines. Thus, the moderate- to large-amplitude deformations of two-dimensional supported bubbles under creeping flow conditions ($Re = 0$) is examined in what follows by numerically computing a series of solutions in the range of capillary numbers $0.005 \leqslant Ca \leqslant 0.5$.

Plots of streamlines for creeping flows past supported bubbles shown in figure 5 make plain that the flow fields are attached and the streamlines conform to the bubble shape until the bubble deformation becomes significant. Here the streamlines, or curves of constant values of the stream function ψ, were found by solving a set of differential
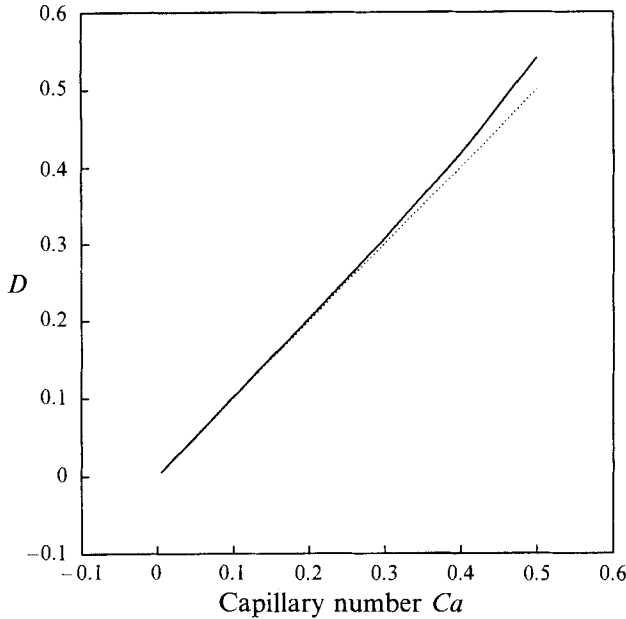
FIGURE 6. Variation of bubble deformation parameter D with Ca when $Re = 0$ for a bubble having the volume of a half-cylinder: ———, finite-element results and $\cdots$, asymptotic result ($15a$).

equations $dy/v = dx/u$ along which $\psi = $ constant (see §4). When bubble deformation is large and the local angle that the free surface makes with the solid wall at the corner corresponding to the rear contact line falls below a critical value ($\doteq 78°$), the flow separates from the free surface and a very weak eddy forms near the rear contact line, in accordance with the well-known result due to Moffatt (1964). As bubble deformation rises, the bubble shape takes on a virtually elliptical profile with the major axis aligning with the direction of principle extension, i.e. with an angle of about 45° with respect to the flow direction. Figure 6 shows that the finite-element prediction of the deformation parameter defined at ($15a$) is in very good agreement with its asymptotic counterpart when Ca is small. However, it is only for very small Ca that the finite-element prediction of the orientation angle agrees with the asymptotic result ($15b$). When Ca is not small, the orientation angle α decreases from 45°, as shown in figure 7. This finding accords with results of extensive studies of fully three-dimensional free bubbles which have found that α falls as Ca rises (cf. Choi & Schowalter 1975). The prediction by Choi & Schowalter is shown in figure 7 by a dotted line for comparison. Although both curves in figure 7 indicate the same decreasing trend of α with Ca, quantitative discrepancy that develops when Ca is relatively large is to be expected given the significant differences in geometric configurations of the two problems.

Equation (14) makes plain that in the limit of small capillary numbers, the bubble deformation is well described by a single harmonic function, $\sin 2\theta$. As Ca increases, not only does the bubble deformation increase but the bubble shape evolves toward more complicated configurations that consist of several harmonic components. To illustrate this fact, computed bubble shapes are decomposed through the harmonic expansion

$$F(\theta) = 1 + \sum_{n=0}^{\infty} a_n \cos n\theta + \sum_{n=1}^{\infty} b_n \sin n\theta. \tag{16}$$

Figure 8 shows the variation of selected coefficients a_n and b_n in (16) as a function of
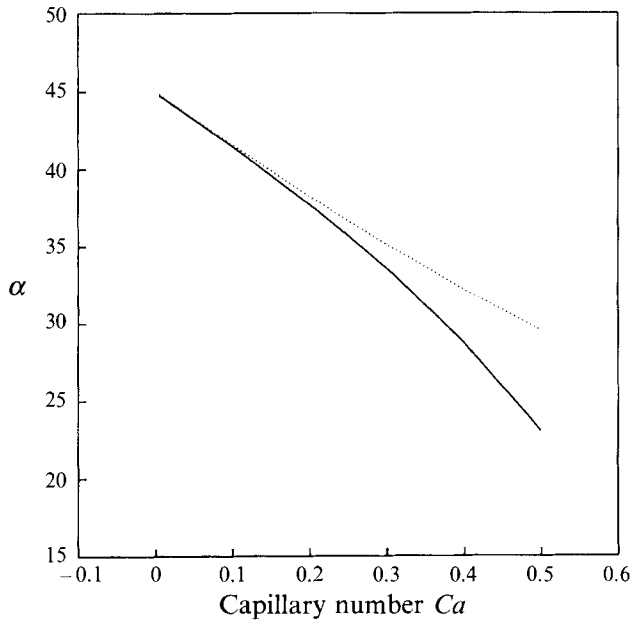
FIGURE 7. Variation of bubble orientation angle α with Ca when $Re = 0$ for a bubble having the volume of a half-cylinder: ———, finite-element results and $\cdots$, asymptotic results of Choi & Schowalter (1975).
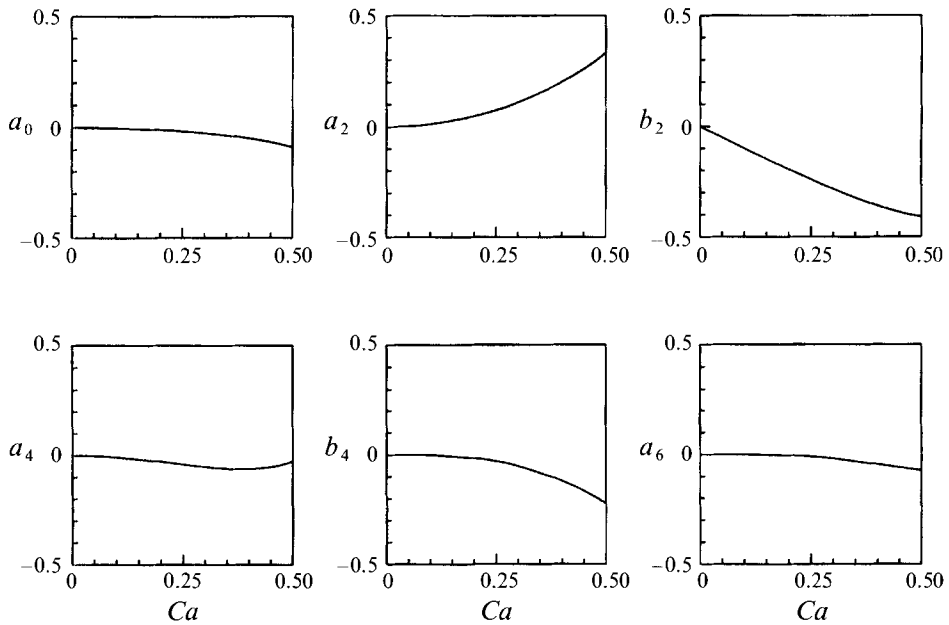

FIGURE 8. Decomposition of the shape of a bubble into harmonic functions as given by (16). Variation with Ca of the first few Fourier-sine and -cosine coefficients a_n and b_n in (16) for a bubble having the volume of a half-cylinder when $Re = 0$.
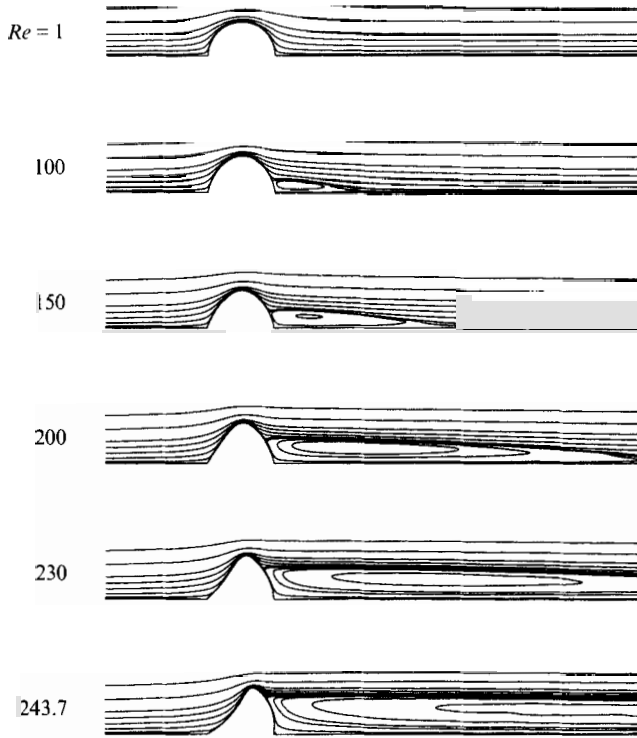
FIGURE 9. Streamlines of flow past a bubble having the volume of a half-cylinder when $Ca = 0.005$ for various Re values. For illustrative purposes, the values of ψ are chosen to be -0.15, -0.1, -0.05, -0.02, -0.01, -0.001, 0, 0.001, 0.01, 0.04, 0.1, 0.2, 0.5 and 1. Not all the streamlines corresponding to negative values of ψ are shown in every case because some of these do not have strong enough recirculating eddies.

Ca. It is noteworthy that all the coefficients in (16) are identically zero when $Ca = 0$ and among all the coefficients only b_2 intersects the ordinate axis, i.e. the vertical line $Ca = 0$, with a non-zero ($= -1$) slope. The latter finding is consistent with the asymptotic result (14) because only b_2 can survive in $dF/d(Ca)$ evaluated at $Ca \to 0$. Moreover, the decomposition (16) has revealed that the computed shapes consist only of harmonics of even indices n; the coefficients of odd harmonics are virtually zero, i.e. they are on the order of truncation error. That the computed shapes consist solely of even harmonics is to be expected and can be explained in terms of standard methods for constructing domain perturbation expansions. Because all terms in the perturbation expansion for the shape function and the stream function at higher orders in Ca, i.e. $O(Ca^2)$ and higher for F and $O(Ca)$ and higher for ψ, are constructed by multiplication of the leading-order (base) solutions that are represented by two harmonics of indices $n = 0$ and $n = 2$, as seen from (13a) and (14), the solution to any order of the expansions must contain only harmonics of even indices. It is interesting to note that all the non-zero coefficients decrease from zero as Ca increases except a_2 which increases from zero with Ca. In order to guarantee that the contact lines remain fixed at $\theta = 0$ and π as the bubble deforms, the coefficients of cosines in (16) must sum to zero. Consequently, it is prohibited for all the cosine coefficients to have the same sign at a given value of Ca, in accord with the results shown in figure 8.
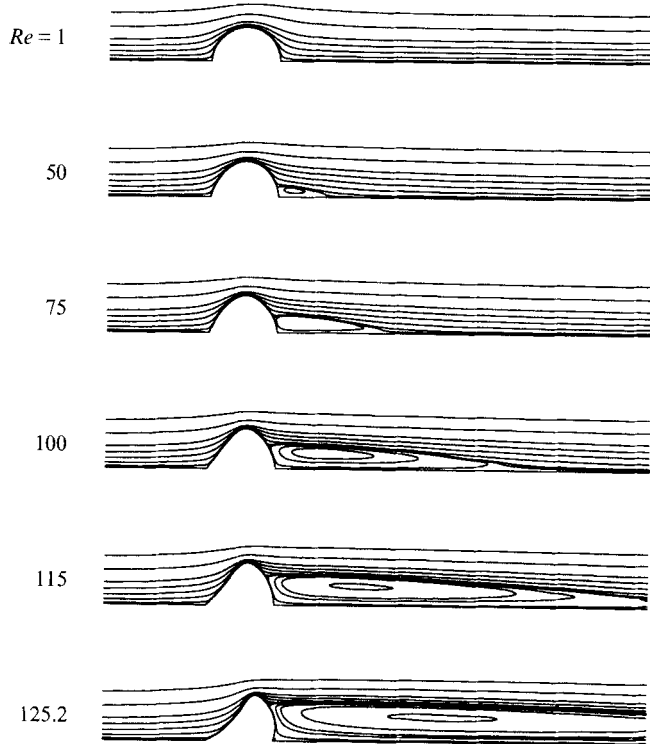
FIGURE 10. Streamlines of flow past a bubble having the volume of a half-cylinder when $Ca = 0.01$ for various Re values. Values of the stream function for which streamlines are shown are the same as those of figure 9.

3.2. *Finite-Reynolds-number cases: $Re \neq 0$ and $V = V_{1/2}$*

To examine bubble response when Re is finite, solutions were computed for fixed values of Ca in the range $0.005 \leqslant Ca \leqslant 0.05$ and for values of Re in the range $0 \leqslant Re \leqslant Re_c$. Here Re_c are the values of the Reynolds numbers at the turning points that signal limits of stability (Iooss & Joseph 1990). Figure 9 shows the evolution with Re of streamlines of flows past supported bubbles when $Ca = 0.005$, corresponding to the case of relatively large surface tension. When $Re = 0$ (Stokes flow), the streamlines retain their fore–aft symmetry around the bubble which exhibits virtually no deformation from the circular profile owing to the effect of large surface tension. At finite Re, however, flow separates from the free surface and a recirculating eddy develops behind the bubble. Evidently, the length of the separated eddy increases significantly with Re but its width remains confined within the level set by the separation point at the free surface. The shape of the separated eddies in a simple shear flow past a supported bubble are in sharp contrast to those in a uniform flow past a circular cylinder (Fornberg 1980) where the width of the eddies also increases with Re. Figure 9 also shows that the deformation of the bubble surface becomes more significant as Re increases. The last bubble profile and flow field shown in figure 9 corresponds to the neutrally stable solution at the turning point where the critical Reynolds number $Re_c = 243.7$. Steady solutions along this shape family do not exist for larger values of Re and beyond the turning point the solution branch folds back to lower values of Re: these are points that are returned to below. Therefore, more than one steady state can exist at a value of $Re < Re_c$. Non-uniqueness of solutions for a given set of boundary conditions is not unusual for a nonlinear system like the present one where nonlinearities arise from the
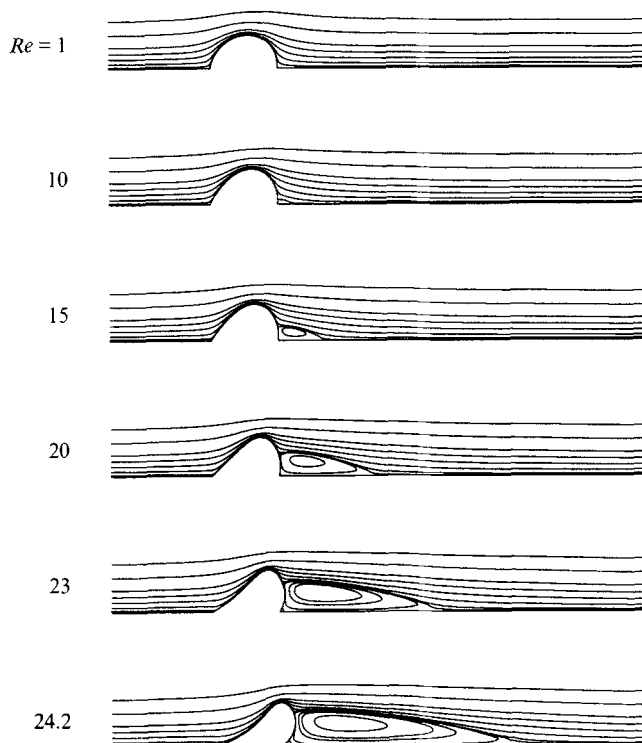
FIGURE 11. Streamlines of flow past a bubble having the volume of a half-cylinder when $Ca = 0.05$ for various Re values. Values of the stream function for which streamlines are shown are the same as those of figure 9.

inertial terms in the Navier–Stokes equations (1) as well as those from the curvature term owing to capillarity in the normal stress condition (4) and the coupling of surface kinematics to the velocity field at the free surface (5).

As Ca is increased to 0.01, corresponding to relatively weaker surface tension than that of figure 9, noticeable bubble deformation occurs and the separated eddy appears at lower Re than when $Ca = 0.005$, as shown in figure 10. The turning point along the solution branch corresponding to $Ca = 0.01$ is also reached at a much lower Re, i.e. $Re_c = 125.2$, than that corresponding to $Ca = 0.005$. If Ca is further increased to 0.05, figure 11 shows that the flow structure and bubble deformations become yet more sensitive to Re than in both the case of $Ca = 0.005$ and that of $Ca = 0.01$. For the case of $Ca = 0.05$, the turning point is reached at $Re_c = 24.2$.

An important feature of the structure of flow fields shown in figures 9–11 is that the appearance or onset of flow separation from the free surface and the size of the separated eddy are not solely determined by Re, unlike the more common situation of viscous boundary-layer separation from a solid boundary. For example, at $Re = 100$ the eddy for $Ca = 0.01$ is much larger than that for $Ca = 0.005$. Also, when $Ca = 0.05$ a sizeable eddy is apparent at $Re = 20$, whereas when $Ca = 0.005$ one is barely visible at $Re = 100$. Therefore, the deformation of the free surface is equally if not more important in generation of separated eddies, a fact that is consistent with the surface vorticity generation mechanism proposed by Ryskin & Leal (1984) and Leal (1989).

Figure 12 shows the solution branches corresponding to the three bubble families of fixed volume having $Ca = 0.005, 0.01$, and 0.05, respectively, in the parameter space of F_{max} versus Re, where F_{max} is the maximum distance from the origin or the centre of
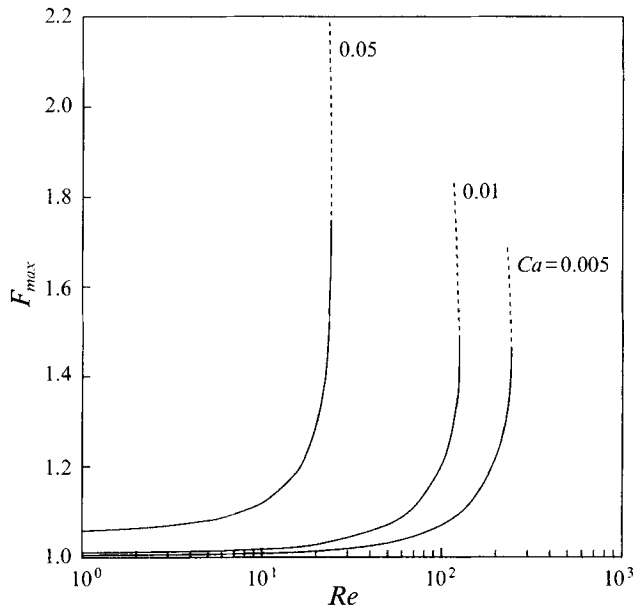
FIGURE 12. Steady-state solution branches of families of bubbles of fixed volume equal to that of a half-cylinder for $Ca = 0.005$, 0.01 and 0.05 in the parameter space of F_{max} as a function of Re: ——, stable solutions and $\cdots$, unstable solutions.

the slot from which the bubble protrudes to the bubble surface. The reason for choosing F_{max} rather than the deformation parameter (15a) used for the case of elliptical deformations is that bubble shapes at finite Reynolds numbers do not have perpendicular 'major' and 'minor' axes. The choice of a simple parameter to completely describe the complicated profiles of bubbles at finite Reynolds numbers is not unique; the choice of F_{max} is only for illustrative purposes. In figure 12, and also in figure 13, solutions that lie along the solid arms or portions of the curves correspond to steady states that are linearly stable and those that lie along the dashed arms of the curves correspond to steady states that are unstable to infinitesimal-amplitude disturbances (Iooss & Joseph 1990). The solution corresponding to that at the turning or limit point is of course a neutrally stable state. Figure 12 shows that at the stability limit (turning point), the critical value of the Reynolds number falls whereas the critical value of the bubble deformation (F_{max}) rises as the capillary number increases. Figure 13 makes plain that as Re increases, the orientation angle α increases at first, reaches a maximum value, and then decreases precipitously as the turning point is approached. For small Ca, e.g. when $Ca = 0.005$, the bubble surface is mostly stretched upward as Re increases and therefore F_{max} so orients that $\alpha \to 90°$ when $Re \gg 1$. This behaviour stands in marked contrast from that in the creeping flow limit where the bubble takes on a smooth elliptical profile with an orientation angle $\alpha \le 45°$. As Ca increases, the bubble surface becomes 'softer' and therefore is deformed more readily. However, because steady states can only exist below a critical Reynolds number Re_c that falls as Ca rises, for larger Ca the deformation component that tends to stretch the bubble upward at $\alpha = 90°$ is weakened and the tendency of the bubble to orient toward smaller values of α becomes stronger. This is also consistent with the results already uncovered under conditions of creeping flow, which show a decrease of α with Ca (cf. figure 7).

Whereas figures 9–13 reveal that the locations of turning points, i.e. values of Re_c, and the structure of the flows at a given Re both vary with Ca, a careful inspection of
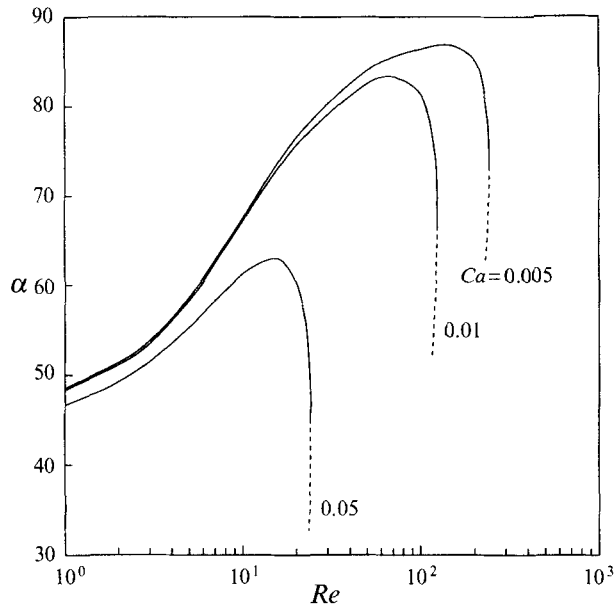
FIGURE 13. Steady-state solution branches of families of bubbles of fixed volume equal to that of a half-cylinder for $Ca = 0.005$, 0.01 and 0.05 in the parameter space of α as a function of Re: ———, stable solutions and $\cdots$, unstable solutions.

Ca	Re_c	We_c
0.005	243.712	1.219
0.01	125.225	1.252
0.05	24.157	1.208

TABLE 1. Critical values of Re and We for various Ca values

Ca	Re	We	x_{sep}	y_{sep}
0.005	200	1	0.71682	0.69319
0.01	100	1	0.77492	0.66192
0.05	20	1	0.97835	0.65850
0.005	240	1.2	0.68506	1.01014
0.01	120	1.2	0.75953	0.90927
0.05	24	1.2	1.17884	0.93480

TABLE 2. Locations of points (x_{sep}, y_{sep}) on the bubble surface from which the flow separates as a function of Ca and Re. Also shown are corresponding values of We

these figures reveals that the location of the turning points and flow structures do not vary significantly with the Weber number $We \equiv Ca\, Re = \rho G^2 L^3/\sigma$. Table 1 shows that the critical values of the Weber number at the turning points We_c are virtually identical for the three families of bubble shapes each of which is characterized by a different value of Ca. Table 2 lists the coordinates of the points on the bubble surfaces (x_{sep}, y_{sep}) from which the flow separates for various values of Ca and Re, along with the corresponding values of We. Clearly, the value of y_{sep} remains virtually constant as Re and Ca vary while keeping their product We fixed. However, at a fixed value of We,
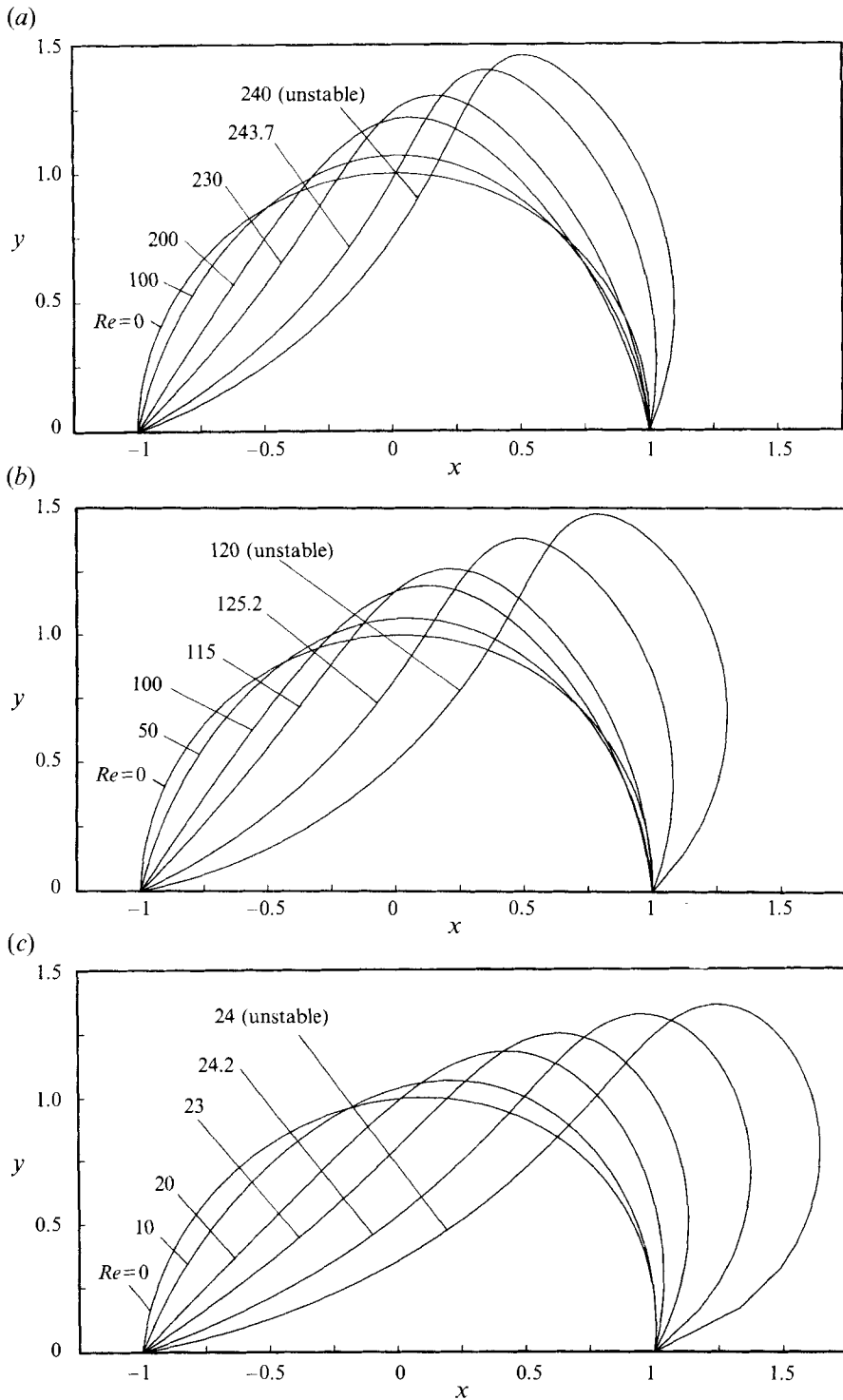
FIGURE 14. Variation of bubble shape profiles with Re when (a) $Ca = 0.005$, (b) $Ca = 0.01$ and (c) $Ca = 0.05$ for a bubble having the volume of a half-cylinder.

x_{sep} increases as Ca increases, a result that accords with earlier observations that tilting of bubbles become more pronounced as capillary number Ca increases. That the Weber number plays a central role or, equivalently, that inertial effects play a more important role than viscous ones, is to be expected because in the present study pronounced variations in the flow structure and the appearance of turning points occur when $Re \gg 1$.

Figure 14 shows the evolution of bubble profiles with Re along steady solution branches of fixed Ca: up to the turning point along the stable arm of the solution branch the bubble deforms more significantly as Re increases and past the turning point it deforms further as Re decreases. Plainly, at least two different deformation components exist at finite Re: one is dominant at low Re and is tantamount to a stretching of the bubble along the direction of principal extension (skewing mode); the other is dominant at large Re and corresponds to an upward stretching of the bubble tip to where the free stream velocity is higher (erecting mode). When Ca is small significant bubble deformation does not occur until Re becomes quite large. Therefore, in this situation the erecting mode is quite noticeable, as shown in figure 14(a). As Ca increases more pronounced bubble deformations arise at smaller Re, such as in figures 14(b) and 14(c), making the skewing mode increasingly more noticeable. Even at a given value of Re, the degree of skewing or erecting of the free surface varies with distance measured from the supporting solid wall (y-coordinate). In the region close to the solid wall the free surface shows more skewing, whereas near the tip, which is far from the solid wall and subject to larger velocities in the simple shear field than the rest of the bubble surface, the free surface exhibits mostly upward stretching. Hence the general feature of shape profiles for $Re \gg 1$ is a skewing toward the downstream direction with the bubble surface possessing a concave front surface and a highly curved tip that erects upward in the y-direction. Figure 14 shows that the rear surface of the bubble is always smoothly curved because below the point on the bubble surface where the flow separates from it the pressure due to surface tension dominates the flow induced stress arising from the rather weak nearby flow in the recirculating eddy. When Re approaches Re_c, however, the bubble shape becomes more skewed, a trend that has already been indicated in figure 13 where it is shown shows that α decreases as $Re \to Re_c$.

To gain further insight into the effect of finite inertia on the evolution of the various deformation modes with Re, it is instructive to decompose computed bubble shapes as in (16). Figure 15 shows the variation of selected coefficients a_n and b_n in (16) as a function of Re when $Ca = 0.01$. Away from the turning point, as Re increases the general trend of bubble deformation is a relatively slow evolution of the 'skewing mode' represented by the negative b_2 and a relatively fast increase of the 'erecting mode' represented by both the negative and decreasing a_2 as well as the positive and increasing a_4. As the turning point is approached, the rate of change of the absolute value of the negative b_2 increases, whereas those of the negative a_2 and the positive a_4 decrease. The variations of the harmonic coefficients depicted in figure 15 as $Re \to Re_c$ are thus consistent with the rapid drop of α with Re shown in figure 13 and the change in the bubble profiles shown in figure 14.

The significant differences in bubble profiles at large and small Re suggest a marked difference in the distributions of normal stress – the sum of pressure and viscous normal stress – on the bubble surfaces. In creeping flows, the form of the pressure distribution is the same as that of viscous normal stress along the bubble surface, as shown by (13c) and (13d). When $Re \gg 1$, pressure rather than viscous normal stress is expected to be the dominant factor that causes a bubble to deform. Indeed, our
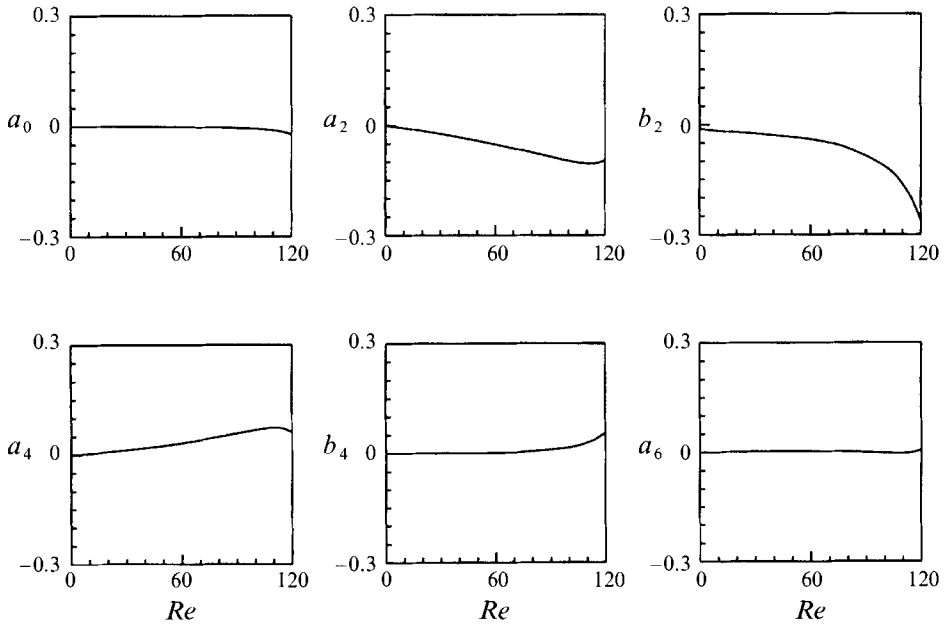
FIGURE 15. Decomposition of the shape of a bubble into harmonic functions as given by (16). Variation with Re of the first few Fourier-sine and -cosine coefficients a_n and b_n in (16) for a bubble having the volume of a half-cylinder when $Ca = 0.01$.

computational results for the case $Ca = 0.01$ shows that the ratio of the peak value of pressure to that of viscous normal stress is about 0.5, 5, 20 and 30 for $Re = 0$, 10, 50 and 100, respectively. Therefore, it is instructive to examine the distribution of pressure on the surfaces of deformed bubbles. Figure 16 shows the evolution of the distribution of pressure on the surface of a bubble with Re at $Ca = 0.01$. For plotting purposes, it is convenient to scale the values of pressure for $Re > 1$ by the Reynolds number Re, which is equivalent to measuring pressure in units of $\rho G^2 L^2$ instead of μG as in the original non-dimensionalization process. As expected, when $Re \leqslant 1$ the pressure profile has two distinct peaks, one positive and the other negative, in accord with the creeping flow solution (13c). When $Re \gg 1$, the positive peak diminishes and the surface pressure distribution develops a large negative peak near the tip ($\theta \sim 90°$) where the flow velocity is greatest. Plainly, this negative pressure peak is responsible for stretching the bubble tip upward. Because of the asymmetric distribution of surface pressure between the front and rear, i.e. pressure in the front is generally higher than that in the rear, the bubble is also caused to skew or tilt in the downstream direction.

At the turning points, the flow induced stresses at the bubble tips become so large that surface tension eventually cannot balance them on as highly curved tips as the bubbles can develop were Re to increase further. Thus, families of fixed bubble volume turn toward lower Reynolds numbers and the bubbles become unstable. Although the transient evolution of the instability is not modelled in this paper, the computed results at the turning points suggest that the breakup process would start from the highly curved tip where the strong negative pressure peak there would tend to tear the bubble surface.

By virtue of the two-dimensionality of the present problem, the flow on the bubble surface is merely a combination of pure extension and pure contraction without surface shear, a unique feature that can render it useful for interfacial rheological
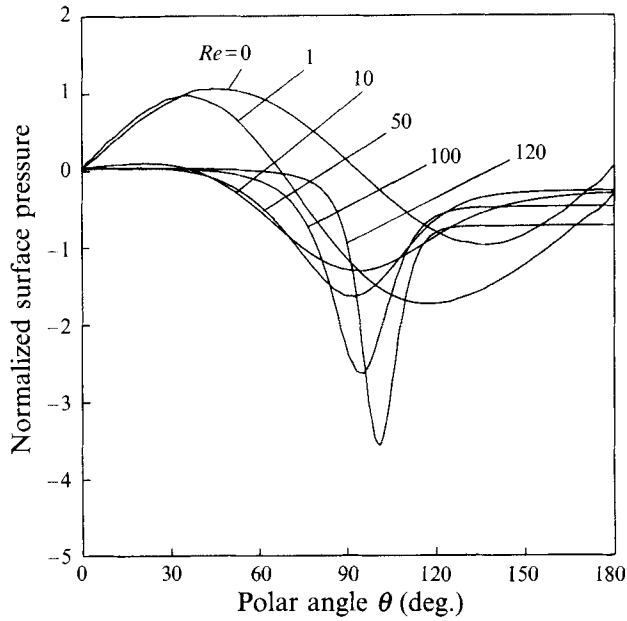
FIGURE 16. Distribution of pressure on the surface of a bubble having the volume of a half-cylinder when $Ca = 0.01$ for various Re values.
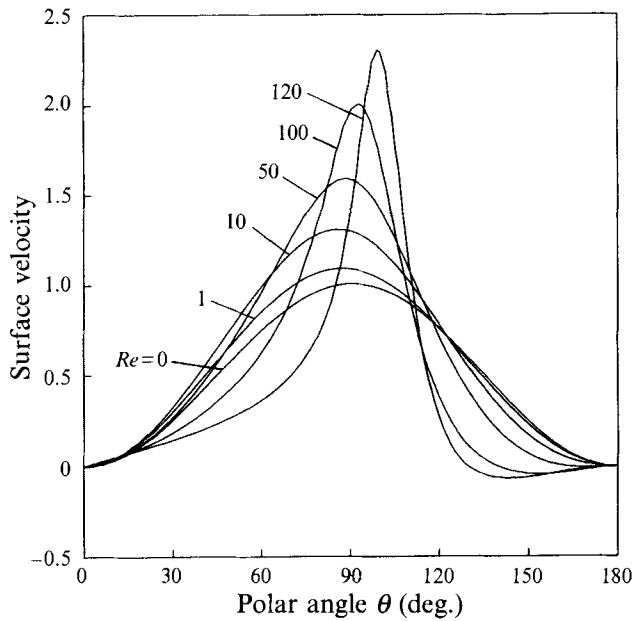

FIGURE 17. Distribution of velocity on the surface of a bubble having the volume of a half-cylinder when $Ca = 0.01$ for various Re values.

measurements. With this application in mind, figure 17 shows the evolution of the tangential velocity distribution on the bubble surface with Re when $Ca = 0.01$. In accord with intuition, the surface velocity typically rises with θ on the front of the bubble, reaches its peak value near the tip, and then falls with θ on the rear of the bubble. The surface flow undergoes pure extension on the front of the bubble and
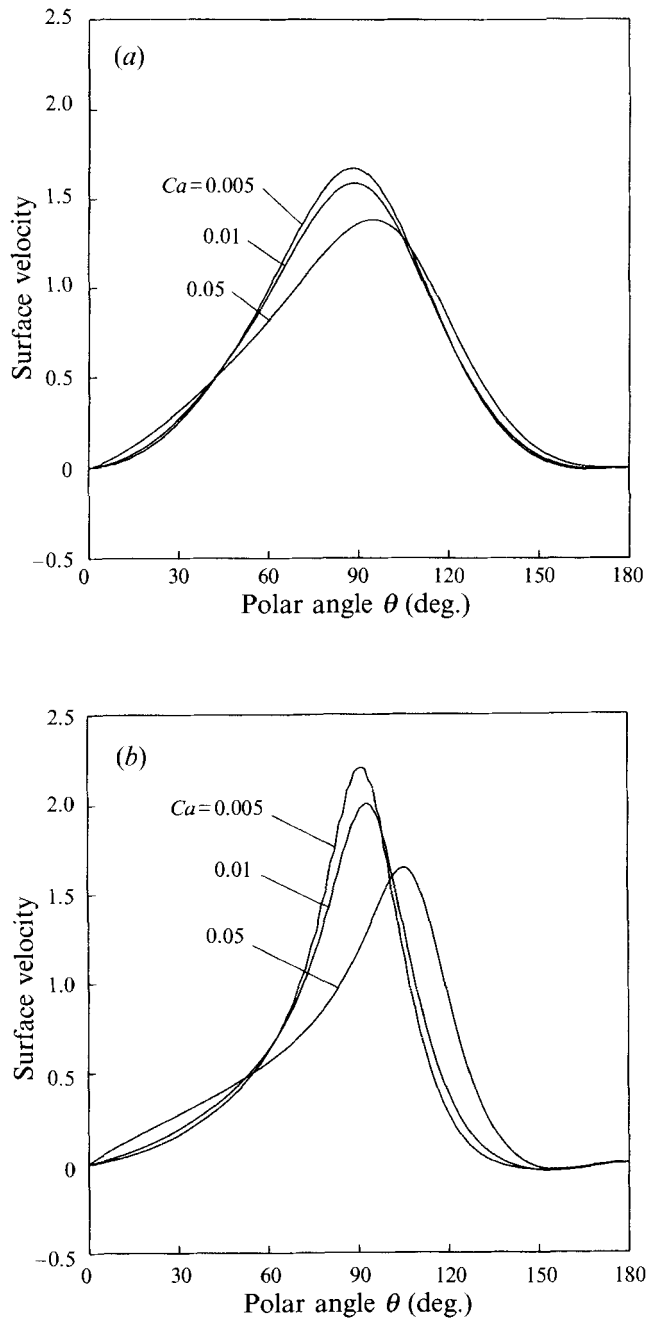
FIGURE 18. Distribution of velocity on the surface of a bubble having the volume of a half-cylinder when (a) $We = 0.5$ and (b) $We = 1$ for various Ca values.

mostly contraction on its rear. When Re is sufficiently large, the separated eddy drives a weak back flow on the bubble surface thus there is some extensional component near the rear contact line. Figure 17 shows that at a fixed value of Ca, both the maximum surface velocity and the surface velocity gradient increase with Re. Figure 18 shows that the surface velocity increases with $We = Ca\,Re$, but its distribution is quite similar at the same value of We. However, at a given We both the maximum surface velocity and
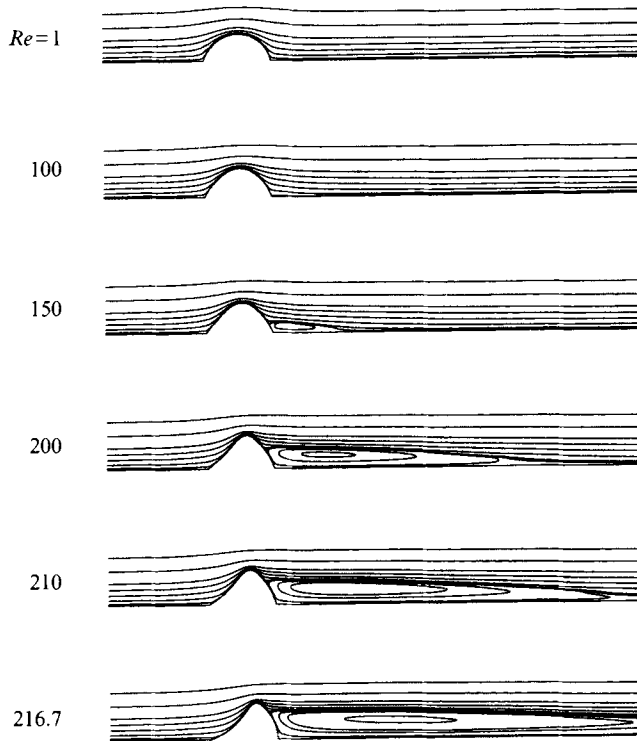
FIGURE 19. Streamlines of flow past a bubble having the volume of $\frac{3}{4}$ of a half-cylinder when $Ca = 0.01$ for various Re values. Values of the stream function for which streamlines are shown are the same as those of figure 9.

surface velocity gradient increase with Re. Hence, in studying interfacial rheological phenomena with the present set-up, increasing We and Re would be effective ways to increase the rate of surface strain. However, it should be kept in mind that both We and Re are confined below their values at the turning points.

3.3. *Bubbles with volumes smaller and greater than that of a half-cylinder: $V \neq V_{1/2}$*

Bubbles of volumes less than that of a half-cylinder are expected to be much easier to maintain in practice because of the stabilizing influence of surface tension. Therefore, figure 19 shows the evolution with Re of streamlines of flows past a supported bubble having a volume of three-quarters that of a half-cylinder, i.e. $V = \frac{3}{4}V_{1/2}$, when $Ca = 0.01$. Plainly, the flow structure and bubble deformation modes follow qualitatively the same trends as those shown earlier in the case of a half-cylinder. Figure 19 shows that when $V = \frac{3}{4}V_{1/2}$, separated eddies of size comparable to those for the case of a half-cylinder and the turning point occur at higher Re than when $V = V_{1/2}$, namely $Re_c = 216.7$ when $V = \frac{3}{4}V_{1/2}$ and $Ca = 0.01$. Although Re (and also We) can be increased to higher values in this case than when $V = V_{1/2}$ before the turning point is reached, the maximum surface velocity (not shown) that can be attained, however, is no more than that of the half-cylinder case. Evidently, this is due to the smaller local liquid velocity that the relatively lower tip of the bubble is exposed to in a simple shear flow.

When the capillary number is held fixed at $Ca = 0.01$ but the bubble volume is increased to five-quarters of a half-cylinder, i.e. $V = \frac{5}{4}V_{1/2}$, the flow structure and bubble deformation modes obtained are qualitatively the same as those when $V = V_{1/2}$
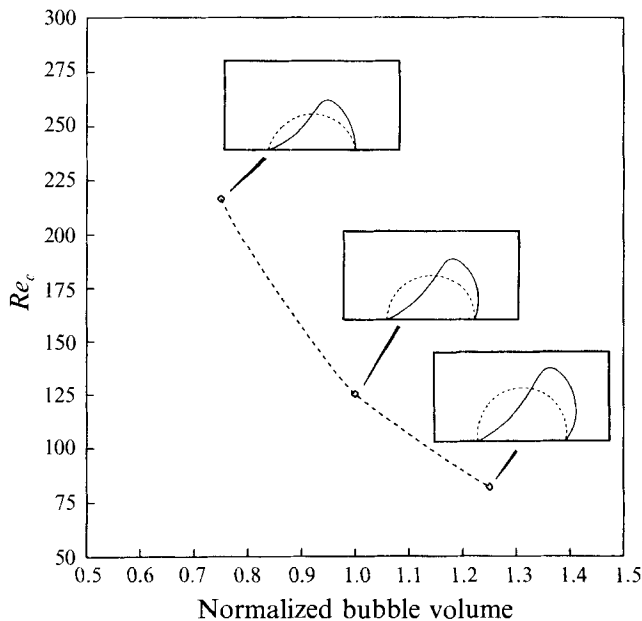
FIGURE 20. Variation of the critical Reynolds number Re_c with normalized bubble volume when $Ca = 0.01$. The bubble volume is normalized by that of a half-cylinder.

and $V = \frac{3}{4}V_{1/2}$, except the turning point occurs at a lower Reynolds number $Re_c \doteq 81.9$; because of this generic nature of the results, streamlines and bubble shapes for the situation when $V = \frac{5}{4}V_{1/2}$ are not shown. The variation of the critical value of the Reynolds number for instability is shown in figure 20 as a function of the bubble volume normalized by that of a half-cylinder, i.e. $V/V_{1/2}$. Figure 20 demonstrates that as bubble volume decreases, the critical Reynolds number for instability increases. The reasons that the rate of change of Re_c with $V/V_{1/2}$ increases as $V/V_{1/2}$ decreases are twofold. First, when $V/V_{1/2}$ decreases, the surface area decreases and the bubble surface is made 'stiffer'. Secondly, when $V/V_{1/2}$ decreases, the bubble surface on the whole experiences lower ambient flow velocities and surface tension is able to keep the bubble stable until higher shear rates, or Reynolds numbers, are reached.

4. Concluding remarks

According to the foregoing results, a supported translationally symmetric cylindrical bubble of fixed volume protruding from a slot into a liquid undergoing a simple shear flow will remain stable with respect to translationally symmetric disturbances until the Reynolds number Re reaches a critical value Re_c. Evidently, such supported bubbles would become unstable when $Re > Re_c$ by rupturing of the interface at the bubble tip where the curvature (radius of curvature) is highest (smallest), although they may succumb sooner to fully three-dimensional disturbances. The breakup of supported bubbles cannot be answered by the steady-state analyses reported in this paper. However, the Galerkin finite element method employed here can be readily extended (see, e.g. Basaran 1992) to analyse the transient evolution of the instability and breakup of supported bubbles.

Based on computational results reported in this paper, the computed solutions are generic because the qualitative features of both the bubble deformation and the

structure of the flow fields vary insignificantly with changes in bubble volume. Intuitively, however, bubbles of volumes smaller than that of a half-cylinder are expected to be easier to maintain as translationally symmetric shapes because surface tension tends to suppress disturbances in the third dimension (z-direction) when $V < V_{1/2}$. For bubbles of volume larger than that of a half-cylinder, surface tension alone can cause a bifurcation from a family of translationally symmetric shapes to one of fully three-dimensional wavy profiles (cf. Brown & Scriven 1980). Whether the flow field can stabilize disturbances in the third dimension cannot of course be answered by the present two-dimensional analysis. Analyses of the problem of bubble stability with respect to general three-dimensional disturbances and the transient process of bubble breakup are issues worthy of attention in their own right and are left open as goals of future research.

The elliptic mesh generation scheme employed in this paper allows tracking of families of bubble shapes of fixed volume to large deformations even when inertial effects are substantial. The results depicted in figures 5, 9–11, and 19 show that it offers other benefits as well. When the Navier–Stokes system is solved in the so-called primitive variable formulation for the components of the velocity at the nodes of the finite element tessellation, nodal values of the stream function are typically obtained by solving a Poisson equation $\nabla^2 \psi = -\omega$, where $\omega \equiv (\partial v / \partial x) - (\partial u / \partial y)$ is the z-component of the vorticity (see, e.g. Lee, Gresho & Sani 1979). The stream function that is so obtained is of course smoothed, in contrast to the stream function that is calculated by the method described in §3 of this paper. By automatically updating the mesh from one parameter step to the next so that the angles formed at the intersections of the sides of the elements are always maintained near 90° (cf. Strang & Fix 1973), the elliptic mesh generator allows the computation of high quality streamlines without the use of any smoothing.

When the bubble shapes are indeed translationally symmetric and the flow field is two-dimensional, the results of this paper show that a steady flow state always exists at an arbitrary value of Re so long as $Ca\,Re = We < 1.2$. Because steady states for large Re can only be obtained for relatively small values of Ca, or relatively strong values of surface tension force, one would not expect to find drastically new behaviour of bubble response and deformation at higher values of Re than those reported in this paper. However, the computational cost of solving for the flow past and the shape of a bubble increases as Re increases because the size of the computational domain and the number of elements use to subdivide it have to rise to maintain computational accuracy. Such high Re calculations are not pursued in this paper. Nevertheless, the flow structure may continue to change with increasing Re. The evolution of the flow structure and the unusual shapes of the recirculating eddies uncovered in this paper as Re becomes very large deserve further detailed study. However, this aspect of the flow problem can be investigated more efficiently and conclusively by considering a fixed boundary problem without having to solve for the unknown shape of the free surface (e.g. Dandy & Leal 1986) and is a goal of future research.

The choice of dimensionless groups used in this paper in presenting the results is by no means unique. The choice of Re and Ca as the pair of dimensionless groups used is natural for two reasons. First, following previous works on viscous free surface flows, it is customary to set $Re = 0$ and vary Ca to explore the effect of 'surface tension' on bubble deformation in creeping flows. Secondly, it is also customary to fix Ca and vary Re to explore the effect of 'inertia' on bubble deformation and flow separation, among other things. In a real experiment, the capillary number $Ca \equiv \mu(GL)/\sigma$ can be held fixed and the Reynold number $Re \equiv \rho(GL)L/\mu$ can be

varied by fixing fluid properties μ and ρ and the product GL but changing the half-width of the slot L. The results can be presented in an alternative and equally useful manner in terms of the pair of dimensionless groups Re and the property number $\mathcal{P} \equiv Re/Ca = \rho L\sigma/\mu^2$. In an experiment, fixing $\mathcal{P}$ and varying Re corresponds to a study in which the motion past a bubble is observed at various shear rates. Yet another future goal of this research is to carry out a systematic set of experiments in which the flow past a supported bubble is examined from both these points of view.

The proposed experiments on supported bubbles in a shear flow can also furnish insights into the phenomenon of migration of the contact line(s) from the sharp edges of the slot when the Gibbs inequality is violated (Oliver *et al.* 1977; see also §1). The finite element methodology outlined and employed in this paper can be extended to account explicitly for the Gibbs inequality, as in the experimental and theoretical study of the 'teapot' effect (Reiner 1956) by Kistler & Scriven (1994).

Although experiments with supported bubbles have direct relevance to diverse situations of immense practical importance in chemical engineering, certain features of the present flow ought to make it extremely useful to fundamental studies on isolating and identifying surface rheological phenomena. The present problem configuration is made particularly attractive because the flow past the cylindrical interface is not only two-dimensional but the surface rate of strain fields on the bubble surface are no more than a combination of pure extensions and pure contractions, i.e. a pure dilatational component. By contrast, with the traditional method involving a shear flow past a three-dimensional free drop or bubble for the measurement of interfacial viscosities, the surface strain field always contains a mixture of shear and dilatation (Wei, Schmidt & Slattery 1974; Philips *et al.* 1980). Moreover, the steady nature of the present flow problem should also render ease to methods for accurate measurement of various dynamic interfacial properties.

REFERENCES

ABBOTT, J. P. 1978 An efficient algorithm for the determination of certain bifurcation points. *J. Comput. Appl. Math.* **4**, 19–27.

ACRIVOS, A. 1983 The breakup of small drops and bubbles in shear flows. *Ann. NY Acad. Sci.* **404**, 1–11.

BARTHES, B. D. & ACRIVOS, A. 1973 Deformation and burst of a liquid droplet freely suspended in a linear shear field. *J. Fluid Mech.* **61**, 1–21.

BASARAN, O. A. 1992 Nonlinear oscillations of viscous liquid drops. *J. Fluid Mech.* **241**, 169–198.

BROWN, R. A. & SCRIVEN, L. E. 1980 On the multiple equilibrium shapes and stability of an interface pinned on a slot. *J. Colloid Interface Sci.* **78**, 528–542.

CHAFFEY, C. E. & BRENNER, H. 1967 A second-order theory for shear deformation of drops. *J. Colloid Sci.* **24**, 258–268.

CHOI, S. J. & SCHOWALTER, W. R. 1975 Rheological properties of nondilute suspensions of deformable particles. *Phys. Fluids* **18**, 420–427.

CHRISTODOULOU, K. N. 1990 Computational physics of slide coating flow. PhD thesis. University of Minnesota. Available from University Microfilms International, Ann Arbor, MI 48106.

CHRISTODOULOU, K. N. & SCRIVEN, L. E. 1989 The fluid mechanics of slide coating. *J. Fluid Mech.* **208**, 321–354.

CHRISTODOULOU, K. N. & SCRIVEN, L. E. 1992 Discretization of free surface flows and other moving boundary problems. *J. Comput. Phys.* **99**, 39–55.

CLIFT, R., GRACE, J. R. & WEBER, M. E. 1978 *Bubbles, Drops and Particles*. Academic.

COX, R. G. 1969 The deformation of a drop in a general time-dependent fluid flow. *J. Fluid Mech.* **37**, 601–623.

DANDY, D. S. & LEAL, L. G. 1986 Boundary-layer separation from a smooth slip surface. *Phys. Fluids* **29** (5), 1360–1366.

DURBIN, P. A. 1988*a* On the wind force needed to dislodge a drop adhered to a surface. *J. Fluid Mech.* **196**, 205–222.

DURBIN, P. A. 1988*b* Free-streamline analysis of deformation and dislodging by wind force of drops on a surface. *Phys. Fluids* **31** (1), 43–48.

DUSSAN V., E. B. & CHOW, R. T.-P. 1983 On the ability of drops or bubbles to stick to non-horizontal surfaces of solids. *J. Fluid Mech.* **137**, 1–29.

FLUMERFELT, R. W. 1980 Effects of dynamic interfacial properties on drop deformation and orientation in shear and extensional flow fields. *J. Colloid Interface Sci.* **76**, 330–349.

FORNBERG, B. 1980 A numerical study of steady viscous flow past a circular cylinder. *J. Fluid Mech.* **98**, 819–855.

FRANKEL, N. A. & ACRIVOS, A. 1970 The constitutive equation for a dilute emulsion. *J. Fluid Mech.* **44**, 65–78.

GIBBS, J. W. 1906 *The Scientific Papers of J. Willard Gibbs. Vol. 1. Thermodynamics*, p. 326. (Reprinted by Dover 1961.)

HOOD, P. 1976 Frontal solution program for unsymmetric matrices. *Intl J. Numer. Meth. Engng* **10**, 379–399 (and Correction, *Intl J. Numer. Meth. Engng* **11** (1977), 1055).

HUYAKORN, P. S., TAYLOR, C., LEE, R. L. & GRESHO, P. M. 1978 A comparison of various mixed interpolation finite elements in the velocity–pressure formulation of Navier–Stokes equations. *Comput. Fluids* **6**, 25–35.

IOOSS, G. & JOSEPH, D. D. 1990 *Elementary Stability and Bifurcation Theory*, 2nd edn. Springer.

KELLER, H. B. 1977 Numerical solution of bifurcation and nonlinear eigenvalue problems. In *Applications of Bifurcation Theory* (ed. P. Rabinowitz), pp. 359–384. Academic.

KING, A. C. & TUCK, E. O. 1993 Thin liquid layers supported by steady air-flow surface traction. *J. Fluid Mech.* **251**, 709–718.

KISTLER, S. F. & SCRIVEN, L. E. 1983 Coating flows. In *Computational Analysis of Polymer Processing* (ed. J. R. A. Pearson & S. M. Richardson), pp. 243–299. Applied Science.

KISTLER, S. F. & SCRIVEN, L. E. 1994 The teapot effect: sheet-forming flows with deflection, wetting and hysteresis. *J. Fluid Mech.* **263**, 19–62.

LEAL, L. G. 1989 Vorticity transport and wake structure for bluff bodies at finite Reynolds number. *Phys. Fluids* A **1**, 124–131.

LEE, R. L., GRESHO, P. M. & SANI, R. L. 1979 Smoothing techniques for certain primitive variable solutions of the Navier–Stokes equations. *Intl. J. Numer. Meth. Engng* **14**, 1785–1804.

MASON, G. 1970 An experimental determination of the stable length of cylindrical liquid bridges. *J. Colloid Interface Sci.* **32**, 172–176.

MOFFATT, H. K. 1964 Viscous and resistive eddies near a sharp corner. *J. Fluid Mech.* **18**, 1–18.

OLIVER, J. F., HUH, C. & MASON, S. G. 1977 Resistance to spreading of liquids by sharp edges. *J. Colloid Interface Sci.* **59**, 568–581.

ORTEGA, J. M. & RHEINBOLDT, W. C. 1970 *Iterative Solution of Nonlinear Equations in Several Variables*. Academic.

PHILIPS, W. J., GRAVES, R. W. & FLUMERFELT, R. W. 1980 Experimental studies of drop dynamics in shear fields: role of dynamic interfacial effects. *J. Colloid Interface Sci.* **76**, 350–370.

POZRIKIDIS, C. 1992 *Boundary Integral and Singularity Methods for Linearized Viscous Flow*. Cambridge University Press.

RALLISON, J. M. 1984 The deformation of small viscous drops and bubbles in shear flows. *Ann. Rev. Fluid Mech.* **16**, 45–66.

RAYLEIGH, LORD 1879 On the capillary phenomena of jets. *Proc. R. Soc. Lond.* **19**, 71–97.

REINER, M. 1956 The teapot effect. *Phys. Today* **9**, 16–20.

RIKS, E. 1972 Application of Newton's method to the problem of elastic stability. *J. Appl. Mech.* **39**, 1060–1065.

RICHARDSON, S. 1968 Two-dimensional bubbles in slow viscous flows. *J. Fluid Mech.* **33**, 476–493.

RUMSCHEIDT, F. D. & MASON, S. G. 1961 Particle motions in sheared suspensions. XII. Deformation and burst of fluid drops in shear and hyperbolic flow. *J. Colloid Sci.* **16**, 238–261.

RYSKIN, G. & LEAL, L. G. 1984 Numerical solution of free-boundary problems in fluid mechanics. Part 2. Buoyancy-driven motion of a gas bubble through a quiescent liquid. *J. Fluid Mech.* **148**, 19–35.

SANTOS, J. M. DE 1991 Two-phase cocurrent downflow through constricted passages. PhD thesis. University of Minnesota. Available from University Microfilms International, Ann Arbor, MI 48106.

STRANG, G. & FIX, G. J. 1973 *An Analysis of the Finite Element Method.* Prentice-Hall.

TAYLOR, G. I. 1934 The formation of emulsions in definable fields of flow. *Proc. R. Soc. Lond.* A **146**, 501–523.

THOMPSON, J. F., WARSI, Z. U. A. & MASTIN, W. C. 1985 *Numerical Grid Generation.* Elsevier.

UNGAR, L. H. & BROWN, R. A. 1982 The dependence of the shape and stability of captive rotating drops on multiple parameters. *Phil. Trans. R. Soc. Lond.* A **306**, 347–370.

WALTERS, R. A. 1980 The frontal method in hydrodynamics simulations. *Comput Fluids* **8**, 265–272.

WEI, L., SCHMIDT, W. & SLATTERY, J. C. 1974 Measurement of the surface dilatational viscosity. *J. Colloid Interface Sci.* **48**, 1–8.

ZAHALAK, G. I., RAO, P. R. & SUTERA, S. P. 1987 Large deformations of a cylindrical liquid-filled membrane by a viscous shear flow. *J. Fluid Mech.* **179**, 283–305.